

The basic character of five two-phase flow model equation sets

W. H. Lee^a and R. W. Lyczkowski^{b,*}

^a *University of California, Los Alamos National Laboratory, Los Alamos, NM, U.S.A.*

^b *Argonne National Laboratory, 9700 South Cass Avenue, Argonne, IL, U.S.A.*

SUMMARY

Three test problems were simulated using five different two-phase flow model equation sets from the open literature. The test problems chosen were a fluidized bed, a batch settling, and a horizontal jet impingement on a vertical wall. These three problems demonstrate an important cross-section of physical phenomena, such as fluidized bed voidage oscillations, phase separation, countercurrent flow, and jet formation. The dispersed flow regime is selected for all three problems. The study was performed to assess the basic character of the five-field equation sets responding to the same initial and boundary conditions and using the same finite difference numerical scheme. The general performance of the five equation sets was found to be similar, even though one of them was ill posed as an initial-value problem. Broad trends are the same and quantitative differences could be assessed by examining the fine structure of the results. None of the equation sets could be entirely rejected on the basis of producing physically impossible or unacceptable results. Copyright © 2000 John Wiley & Sons, Ltd.

KEY WORDS: batch settling; fluidized bed; ill-posed PDEs; jet impingement; two-phase models; well-posed PDEs

1. INTRODUCTION

In recent years, research has increased concerning the development of two-phase flow model equations; some of these equation systems possess complex characteristics. The full implications of the complex characteristics are still not completely agreed upon, but many investigators agree that the equations are probably ill posed as an initial-value or Cauchy problem. Certainly they are not completely hyperbolic, which causes numerical difficulties because the von Neumann analysis for the linear system predicts exponential growth. *Ad hoc* numerical techniques using space increments or interfacial drag sufficiently large to stabilize some unstable modes have recently been suggested.

* Correspondence to: Argonne National Laboratory, 9700 South Cass Avenue, Argonne, IL 60439, U.S.A.

It now appears that the modeling difficulties arise from constitutive models and assumptions concerning the treatment of the pressure, stress, and transient flow forces at the interface between the phases or inconsistent approximations. Stuhmiller [1] presented an analysis that tended to support the importance of the interfacial pressure modeling by obtaining the averaged equation of motion for a single accelerating sphere that has real characteristics. Banerjee *et al.* [2] admitted two-phase pressures into their model by adopting an interphase pressure difference constitutive equation and also obtained all real characteristics. Gidaspow [3], on the other hand, showed that a consistent thermodynamic approach would also produce two-phase model equations having all real characteristics.

The objective of this paper is to present the computational results of five transient two-phase flow models, all solved using the same finite differencing technique, numerical scheme, and computer code structure [4]. The problems analyzed are

1. One-dimensional fluidized bed.
2. One-dimensional vertical batch settling of a two-phase mixture.
3. Horizontal two-phase jet impingement on a vertical wall.

The one-dimensional fluidized bed problem was chosen because data are available concerning the frequency of voidage oscillations. The batch settling problem demonstrates the propagation of density or kinematic waves and phase separation, which has been analyzed by Soo [5]. The two-phase jet impingement problem can be compared with experimental data [6]. The five sets of equations under consideration are

1. Soo's model [7].
2. Gidaspow's model [3].
3. The Rudinger–Chang model [8], as modified by Lyczkowski [9].
4. The Hancox *et al.* model [10].
5. The ill-posed model [11] that is the same as the TRAC [12] code vessel model.

These five two-phase models represent a diversified and representative cross-section of active research. The first four models were chosen because they all explicitly attempted to develop well-posed two-phase models to remedy the ill-posed model, which is widely used in two-phase analysis [11]. Gidaspow's model was developed for fluidized beds. Arastoopour and Gidaspow analyzed four two-phase models for steady state one-dimensional vertical pneumatic conveying of solids [13]. The results of the computations from each of the five models are compared with the available analytical results, with available data and against each other.

2. TWO-PHASE FLOW MODEL EQUATIONS

This section presents the five different two-phase flow equation sets under consideration. In the interest of compactness, it is best to begin this section with the equation set, which we will refer to as the 'basic' or 'ill-posed' set [11]. In this section when we refer to an equation set as being ill-posed or well-posed, we refer to whether the characteristics for one-dimensional, incompressible ($\rho_i, \rho_j = \text{constant}$), 'potential type' [11], and isothermal flow are either complex valued or real. They are summarized in Appendix B. When the phases are compressible, the

polynomial for the characteristics does not factor in general. In this case, much more effort is needed to determine the characteristics numerically [11]. Modifications of this basic set will then be given for each of the subsequent four sets. The governing equations of mass and momentum in two-dimensional Cartesian geometry are given by

2.1. Basic equation set

Continuity

$$\frac{\partial}{\partial t} (\alpha_i \rho_i) + \frac{\partial}{\partial x} (\alpha_i \rho_i u_i) + \frac{\partial}{\partial y} (\alpha_i \rho_i v_i) = (\Gamma_c - \Gamma_e) \quad (1)$$

$$\frac{\partial}{\partial t} (\alpha_j \rho_j) + \frac{\partial}{\partial x} (\alpha_j \rho_j u_j) + \frac{\partial}{\partial y} (\alpha_j \rho_j v_j) = (\Gamma_e - \Gamma_c) \quad (1a)$$

x-Direction momentum

$$\frac{\partial}{\partial t} (\alpha_i \rho_i u_i) + \frac{\partial}{\partial x} (\alpha_i \rho_i u_i u_i) + \frac{\partial}{\partial y} (\alpha_i \rho_i v_i u_i) + \alpha_i \frac{\partial P}{\partial x} - K(u_j - u_i) - (\Gamma_c u_j - \Gamma_e u_i) = 0 \quad (2)$$

$$\frac{\partial}{\partial t} (\alpha_j \rho_j u_j) + \frac{\partial}{\partial x} (\alpha_j \rho_j u_j u_j) + \frac{\partial}{\partial y} (\alpha_j \rho_j v_j u_j) + \alpha_j \frac{\partial P}{\partial x} - K(u_i - u_j) - (\Gamma_e u_i - \Gamma_c u_j) = 0 \quad (2a)$$

y-Direction momentum

$$\frac{\partial}{\partial t} (\alpha_i \rho_i v_i) + \frac{\partial}{\partial x} (\alpha_i \rho_i u_i v_i) + \frac{\partial}{\partial y} (\alpha_i \rho_i v_i v_i) + \alpha_i \frac{\partial P}{\partial y} - K(v_j - v_i) - (\Gamma_c v_j - \Gamma_e v_i) + \alpha_i \rho_i g = 0 \quad (3)$$

$$\frac{\partial}{\partial t} (\alpha_j \rho_j v_j) + \frac{\partial}{\partial x} (\alpha_j \rho_j u_j v_j) + \frac{\partial}{\partial y} (\alpha_j \rho_j v_j v_j) + \alpha_j \frac{\partial P}{\partial y} - K(v_i - v_j) - (\Gamma_e v_i - \Gamma_c v_j) + \alpha_j \rho_j g = 0 \quad (3a)$$

In Equations (1)–(3a) above, *i* refers to the liquid or solid phase and *j* refers to the gas or vapor phase. Gravity is assumed to act in the *y*-direction. The volume fractions are constrained by

$$\alpha_i + \alpha_j = 1 \quad (4)$$

since there are never more than two co-existent phases. The drag function *K* and evaporation and condensation rates are flow regime-dependent. They are given in Section 3.

The energy equations are given by

$$\begin{aligned} & \frac{\partial}{\partial t} (\alpha_i \rho_i h_i) + \frac{\partial}{\partial x} (\alpha_i \rho_i u_i h_i) + \frac{\partial}{\partial y} (\alpha_i \rho_i v_i h_i) \\ &= \alpha_i \left(\frac{\partial P}{\partial t} + u_i \frac{\partial P}{\partial x} + v_i \frac{\partial P}{\partial y} \right) + R_i (T_j - T_i) + (\Gamma_c - \Gamma_e) h_j \end{aligned} \tag{5}$$

$$\begin{aligned} & \frac{\partial}{\partial t} (\alpha_j \rho_j h_j) + \frac{\partial}{\partial x} (\alpha_j \rho_j u_j h_j) + \frac{\partial}{\partial y} (\alpha_j \rho_j v_j h_j) \\ &= \alpha_j \left(\frac{\partial P}{\partial t} + u_j \frac{\partial P}{\partial x} + v_j \frac{\partial P}{\partial y} \right) + R_j (T_i - T_j) + (\Gamma_e - \Gamma_c) h_j + \left(K + \frac{\Gamma_e - \Gamma_c}{2} \right) [(u_i - u_j)(v_i - v_j)] \end{aligned} \tag{5a}$$

The continuity and energy equations will be taken to be common to all five of the equation sets. Only the momentum equations change from set to set. The internal shear and thermal conductivity have been taken to be zero so that we have ‘potential type’ flow [11]. The densities for each phase are given by

$$\rho_i, \rho_j = \rho_i(P, h_i), \rho_j(P, h_j) \tag{6}$$

or

$$\rho_i, \rho_j = \text{constant} \tag{6a}$$

depending on the problem. Equations (1)–(3a) possess a complex conjugate pair of characteristics in one dimension given by Equation (B1) and are therefore ill posed as an initial-value problem. The usual assumption has been made that the phase pressures are equal [11]. The momentum equation set, involving pressure times vapor volume fraction gradients, and no additional terms, is not under consideration; however, it is discussed by Lyczkowski *et al.* [11]. Arastoopour and Gidaspow found this set to be physically unacceptable for one-dimensional steady flows [13].

2.2. Soo’s momentum equations

The two-dimensional dispersed Brownian motion flow form of Soo’s [7] momentum equations is given by

x-Direction momentum

RHS of Equation (2)

$$-P \frac{\partial \alpha_i}{\partial x} + \frac{\partial}{\partial x} [\rho_i \alpha_i (u_m - u_i)^2] + \frac{\partial}{\partial y} [\alpha_i \rho_i (u_m - u_i)(v_m - v_i)] \tag{7}$$

RHS of Equation (2a)

$$-P \frac{\partial \alpha_j}{\partial x} + \frac{\partial}{\partial x} [\alpha_j \rho_j (u_m - u_j)^2] + \frac{\partial}{\partial y} [\alpha_j \rho_j (u_m - u_j)(v_m - v_j)] \quad (7a)$$

y-Direction momentum

RHS of Equation (3)

$$-P \frac{\partial \alpha_j}{\partial y} + \frac{\partial}{\partial x} [\rho_j \alpha_i (v_m - v_i)(u_m - u_i)] + \frac{\partial}{\partial y} [\alpha_i \rho_i (v_m - v_i)^2] \quad (8)$$

RHS of Equation (3a)

$$-P \frac{\partial \alpha_j}{\partial y} + \frac{\partial}{\partial x} [\rho_j \alpha_j (v_m - v_j)(u_m - u_j)] + \frac{\partial}{\partial y} [\alpha_j \rho_j (v_m - v_j)^2] \quad (8a)$$

where

$$\rho_m u_m = \alpha_i \rho_i u_i + \alpha_j \rho_j u_j \quad (9)$$

$$\rho_m v_m = \alpha_i \rho_i v_i + \alpha_j \rho_j v_j \quad (10)$$

and

$$\rho_m = \alpha_i \rho_i + \alpha_j \rho_j \quad (11)$$

When these equations are added together for each direction they become

Mixture momentum equations

$$\frac{\partial}{\partial t} (\rho_m u_m) + \frac{\partial}{\partial x} (\rho_m u_m u_m) + \frac{\partial}{\partial y} (\rho_m v_m u_m) + \frac{\partial P}{\partial x} = 0 \quad (12)$$

and

$$\frac{\partial}{\partial t} (\rho_m v_m) + \frac{\partial}{\partial x} (\rho_m u_m v_m) + \frac{\partial}{\partial y} (\rho_m v_m v_m) + \frac{\partial P}{\partial y} = -\rho_m g \quad (12a)$$

The mixture momentum equations given by Equations (12) and (12a) are identical in form to the inviscid single-phase momentum equations. This set of equations is hyperbolic [7]. The characteristics are given by Equations (B2)–(B6).

2.3. Extended 'Rudinger–Chang' momentum equations

The Rudinger–Chang [8] momentum equations as modified by Lyczkowski [9] are given by

x-Direction momentum

$$\text{RHS of Equation (2)} \quad \left\{ \begin{array}{l} -\alpha_j \frac{\partial P}{\partial x} \quad 0 < \alpha_j < 0.5 \\ +\alpha_i \frac{\partial P}{\partial x} \quad 1 > \alpha_j \geq 0.5 \end{array} \right. \quad (13)$$

$$\text{RHS of Equation (2a)} \quad \left\{ \begin{array}{l} +\alpha_j \frac{\partial P}{\partial x} \quad 0 < \alpha_j < 0.5 \\ -\alpha_i \frac{\partial P}{\partial x} \quad 1 > \alpha_j \geq 0.5 \end{array} \right. \quad (13a)$$

y-Direction momentum

$$\text{RHS of Equation (3)} \quad \left\{ \begin{array}{l} -\alpha_j \frac{\partial P}{\partial y} \quad 0 < \alpha_j < 0.5 \\ +\alpha_i \frac{\partial P}{\partial y} \quad 1 > \alpha_j \geq 0.5 \end{array} \right. \quad (14)$$

$$\text{RHS of Equation (3a)} \quad \left\{ \begin{array}{l} +\alpha_j \frac{\partial P}{\partial y} \quad 0 < \alpha_j < 0.5 \\ -\alpha_i \frac{\partial P}{\partial y} \quad 1 > \alpha_j \geq 0.5 \end{array} \right. \quad (14a)$$

These equations are hyperbolic. The characteristics are given by Equations (B7) and (B8).

2.4. Hancox et al. momentum equations

These momentum equations were developed for so-called mixed flow by extending analytical relations derived by Stuhmiller [1] for a single accelerating sphere [10]. The basic assumption is that the average phase pressures are equal but different from the interfacial pressure. These equations are, in two dimensions

x-Direction

RHS of Equation (2)

$$-C_p \rho_c (u_d - u_c)^2 \frac{\partial \alpha_i}{\partial x} + \frac{1}{2} \alpha_d \rho_c \left[\frac{\partial}{\partial t} (u_c - u_d) + u_d \frac{\partial}{\partial x} (u_c - u_d) + v_d \frac{\partial}{\partial y} (u_c - u_d) \right] \quad (15)$$

RHS of Equation (2a)

$$-C_p \rho_c (u_d - u_c)^2 \frac{\partial \alpha_j}{\partial x} + \frac{1}{2} \alpha_d \rho_c \left[\frac{\partial}{\partial t} (u_c - u_d) + u_d \frac{\partial}{\partial x} (u_c - u_d) + v_d \frac{\partial}{\partial y} (u_c - u_d) \right] \quad (15a)$$

y-Direction

RHS of Equation (3)

$$-C_p \rho_c (v_d - v_c)^2 \frac{\partial \alpha_j}{\partial y} + \frac{1}{2} \alpha_d \rho_c \left[\frac{\partial}{\partial t} (v_c - v_d) + u_d \frac{\partial}{\partial x} (v_c - v_d) + v_d \frac{\partial}{\partial y} (v_c - v_d) \right] \quad (16)$$

RHS of Equation (3a)

$$-C_p \rho_c (v_d - v_c)^2 \frac{\partial \alpha_j}{\partial y} - \frac{1}{2} \alpha_d \rho_c \left[\frac{\partial}{\partial t} (v_c - v_d) + u_d \frac{\partial}{\partial x} (v_c - v_d) + v_d \frac{\partial}{\partial y} (v_c - v_d) \right] \quad (16a)$$

In Equations (15)–(16a), the subscripts c and d denote continuous and dispersed phases respectively with the identification

$$\left. \begin{array}{l} c = i \\ d = j \end{array} \right\} \text{ for } 0 < \alpha_j < 0.5 \quad (17)$$

and

$$\left. \begin{array}{l} c = j \\ d = i \end{array} \right\} \text{ for } 1 > \alpha_j \geq 0.5$$

The model used for C_p is from Stuhmiller [1] and is given by

$$C_p = 0.37 C_d \quad (18)$$

where C_d is the single sphere drag function. We used $C_d = 0.42$ (fully turbulent flow) so that the value of $C_p = 0.155$. This set of equations is hyperbolic for incompressible flow as long as [10]

$$\frac{4C_p \rho_c (\rho^* + C^*) + \alpha_d^2 C^{*2}}{4\alpha_c \alpha_d \rho_c (\rho_d + C^*)} > 1 \quad (19)$$

where

$$C^* = \frac{1}{2} \rho_c / \alpha_c \quad (19a)$$

and

$$\rho^* = \alpha_c \rho_d + \alpha_d \rho_c \quad (19b)$$

The characteristics are given by Equations (B9)–(B12).

2.5. Gidaspow's momentum equations

These equations, given by a mixture momentum equation and a relative velocity constitutive equation [3], were extended to two dimensions by Shih and Arastoopour [14]. They may be cast into the forms given by Equations (2) and (3) by subtracting the relative velocity equation times $\alpha_j \rho_j$ from the mixture momentum for phase i and using the mixture momentum equation for phase j . This manipulation results in the following, including mass transfer:

x-Direction

RHS of Equation (2)

$$-\alpha_j \frac{\partial P}{\partial x} - \alpha_j \rho_j \left[\frac{\partial u_j}{\partial t} + (u_j - u_i) \frac{\partial u_i}{\partial x} + u_i \frac{\partial u_j}{\partial x} + (v_j - v_i) \frac{\partial u_i}{\partial y} + v_i \frac{\partial u_j}{\partial y} \right] - u_j (\Gamma_c - \Gamma_c) \quad (20)$$

RHS of Equation (2a)

$$-\alpha_i \frac{\partial P}{\partial x} - \alpha_i \rho_i \left[\frac{\partial u_i}{\partial t} + u_i \frac{\partial u_i}{\partial x} + v_i \frac{\partial u_i}{\partial y} \right] - u_i (\Gamma_c - \Gamma_c) - K(u_i - u_j) \quad (20a)$$

y-Direction

RHS of Equation (3)

$$-\alpha_j \frac{\partial P}{\partial y} - \alpha_j \rho_j \left[\frac{\partial v_j}{\partial t} + (u_j - u_i) \frac{\partial v_i}{\partial x} + u_i \frac{\partial v_j}{\partial x} + (v_j - v_i) \frac{\partial v_i}{\partial y} + v_i \frac{\partial v_j}{\partial y} \right] + v_j (\Gamma_c - \Gamma_c) \quad (21)$$

RHS of Equation (3a)

$$-\alpha_i \frac{\partial P}{\partial y} - \alpha_i \rho_i \left[\frac{\partial v_i}{\partial t} + u_i \frac{\partial v_i}{\partial x} + v_i \frac{\partial v_i}{\partial y} \right] - v_i (\Gamma_c - \Gamma_c) - K(v_i - v_j) \quad (21a)$$

These equations are hyperbolic [3,15]. The characteristics are given by Equations (B13) and (B14).

3. THE DRAG FUNCTION AND PHASE CHANGE RATES

In order to close the set of equations, one needs the additional information, i.e., the three interface jump conditions (interfacial mass, momentum, and heat transfers), and the additional boundary conditions.

The above mass, momentum, and energy equations are solved as an initial and boundary value problem to obtain $\alpha_i, \alpha_j, P, u_i, v_i, u_j, v_j, h_i,$ and h_j . The densities ρ_i and ρ_j are provided through the use of the equation of state (6) or (6a).

In general, the drag function K is dependent on the flow regime, local vapor volume fraction, vapor and liquid density, Reynolds' number, and phase velocity. There are two models of K function used in the computer program. One is given by [15]

$$K = Cf(\alpha_j)$$

where C is some coefficient and

$$f(\alpha_j) = \begin{cases} 1 + 10^{2000(0.01 - \alpha_j)}, & \text{when } 0 < \alpha_j \leq 0.01 \\ 1, & \text{when } 0.01 < \alpha_j < 0.99 \\ 1 + 10^{2000(\alpha_j - 0.09)}, & \text{when } 1 > \alpha_j \geq 0.99 \end{cases} \quad (23)$$

A more elaborate form of K was used in this study, given by [4,16]

$$K = 0.375(\rho'_i + \rho'_j) \left\{ C_d |\vec{U}_i - \vec{U}_j| + \frac{12[\alpha_i \mu_i / \rho_i + (1 - \alpha_i) \mu_j / \rho_j]}{r_p} \right\} A(\alpha_j, N) \quad (24)$$

where

$$A = \begin{cases} \alpha_j^{2/3} \left(\frac{4\pi N}{3} \right)^{1/3}, & \text{when } \alpha_j \leq 1/2 \\ (1 - \alpha_j)^{2/3} \left(\frac{4\pi N}{3} \right)^{1/3}, & \text{when } \alpha_j > 1/2 \end{cases} \quad (25)$$

$$r_p = \begin{cases} \left(\frac{3\alpha_j}{4\pi N} \right)^{1/3}, & \text{when } \alpha_j \leq 1/2 \\ \left[\frac{3(1 - \alpha_j)}{4\pi N} \right]^{1/3}, & \text{when } \alpha_j > 1/2 \end{cases} \quad (26)$$

The evaporation and condensation rates Γ_e and Γ_c are determined from [4]

$$\begin{aligned} \Gamma_e &= \lambda_c \rho_i \alpha_i (T_i - T_s) / T_s & \text{for } T_i \geq T_s \\ &= 0 & \text{for } T_i < T_s \end{aligned} \quad (27)$$

$$\begin{aligned} \Gamma_c &= \lambda_c \rho_j \alpha_j (T_s - T_j) / T_s & \text{for } T_j \leq T_s \\ &= 0 & \text{for } T_j > T_s \end{aligned} \quad (28)$$

where λ_e and λ_c are time relaxation parameters with unit s^{-1} . For the tested problem described in this paper, λ_e and λ_c are set equal to 0.1.

For the dispersed flow regime, the interfacial heat transfer coefficients, R_i and R_j are calculated from [17]

$$R_i = 8.067 \frac{k_i}{r_p} \quad (29)$$

for the liquid phase and

$$R_j = \frac{1}{r_p} (1 + 0.37 Re^{0.5} Pr_j^{0.33}) \quad (30)$$

for the vapor phase, where

$$Re = \frac{2\rho_j |\vec{U}_i - \vec{U}_j| r_p}{\mu_j} \quad (31)$$

and

$$Pr = \frac{C_{p,j} \mu_j}{k_j} \quad (32)$$

The correlations R_j and R_i are obtained with r_p defined by Equation (26).

4. NUMERICAL SOLUTION PROCEDURE

The finite difference equations of mass, momentum, and energy are solved as an initial value problem in time and a boundary value problem in space. The procedure is iterative and the main steps necessary to determine the flow conditions at time $t + \Delta t$ from those at time t are as follows:

1. The pressure distribution at the time $t + \Delta t$ is guessed.
2. The momentum equations are solved to compute the first approximation of the two velocity components for each of the two phases.
3. Partial energy equations are solved for approximating enthalpies of both phases.
4. Densities and temperatures of both phases are calculated using equation of state and estimated enthalpies and pressures.
5. Liquid volume fraction α_i is estimated from the continuity equation of liquid. Gas volume fraction α_j is then calculated from the relation $\alpha_j = 1 - \alpha_i$.
6. It is now checked to see if the gas continuity equation is satisfied. If the equation is not satisfied, then pressure is corrected, the amount of correction being dependent on the mass residual, and steps 2–6 are repeated. This iterative procedure is continued until the mass residual is less than the specified value.

7. Energy equations are solved for enthalpies. Temperatures and densities are then calculated using the equations of state.
8. A new time step is chosen and steps 1–7 are repeated.

The numerical scheme used in the pressure calculation is

$$P^{\beta+1} = P^\beta - \omega_j \frac{D_j^\beta}{(\partial D_j / \partial P)^\beta}, \quad \text{when } \alpha_j \geq \alpha^* \tag{33}$$

and

$$P^{\beta+1} = P^\beta - \omega_i \frac{D_i^\beta}{(\partial D_i / \partial P)^\beta}, \quad \text{when } \alpha_i < \alpha^* \tag{34}$$

where α^* is an input constant, e.g., $\alpha^* = 0.001$. In the pressure iteration loop, i.e., Equations (33) and (34), the relaxation factors ω_i and ω_j are set to 0.95, since we use Jacobi’s method for the relaxation procedure, which requires that $0 < \omega \leq 1.0$. D_j^β and D_i^β are the residue masses from the continuity equations for j and i phases at iteration step β . The definitions of D_j and D_i are given by

$$\begin{aligned} (D_j)_{\zeta,\eta}^\beta &= \left(\frac{1}{\delta t}\right)[(\rho'_j)_{\zeta,\eta}^\beta - (\rho'_j)_{\zeta,\eta}^{\beta-1}] + \left(\frac{1}{\delta x}\right)[(\rho'_j u_j)_{\zeta+1/2,\eta}^\beta - (\rho'_j u_j)_{\zeta-1/2,\eta}^\beta] \\ &\quad + \left(\frac{1}{\delta y}\right)[(\rho'_j v_j)_{\zeta,\eta+1/2}^\beta - (\rho'_j v_j)_{\zeta,\eta-1/2}^\beta] \end{aligned} \tag{35}$$

and

$$\begin{aligned} (D_i)_{\zeta,\eta}^\beta &= \left(\frac{1}{\delta t}\right)[(\rho'_i)_{\zeta,\eta}^\beta - (\rho'_i)_{\zeta,\eta}^{\beta-1}] + \left(\frac{1}{\delta x}\right)[(\rho'_i u_i)_{\zeta+1/2,\eta}^\beta - (\rho'_i u_i)_{\zeta-1/2,\eta}^\beta] \\ &\quad + \left(\frac{1}{\delta y}\right)[(\rho'_i v_i)_{\zeta,\eta+1/2}^\beta - (\rho'_i v_i)_{\zeta,\eta-1/2}^\beta] \end{aligned} \tag{36}$$

The momentum exchange terms $K(\vec{U}_i - \vec{U}_j)$ and $K(\vec{U}_j - \vec{U}_i)$ in the liquid and vapor momentum equations respectively are neglected in calculating Equations (33) and (34). It is found that these formulations result in greater stability for the pressure calculations for the problems that have been investigated so far. The expressions of these two derivatives with the finite difference grid shown in Figure 1 are

$$\frac{\partial D_i}{\partial P} = \frac{1}{(\partial P / \partial \rho'_i)_{\zeta,\eta} \delta t} + \frac{\delta t [(\alpha_i)_{\zeta+1/2,\eta} + (\alpha_i)_{\zeta-1/2,\eta}]}{(\delta x)^2} + \frac{\delta t [(\alpha_i)_{\zeta,\eta+1/2} + (\alpha_i)_{\zeta,\eta-1/2}]}{(\delta y)^2} \tag{37}$$

and

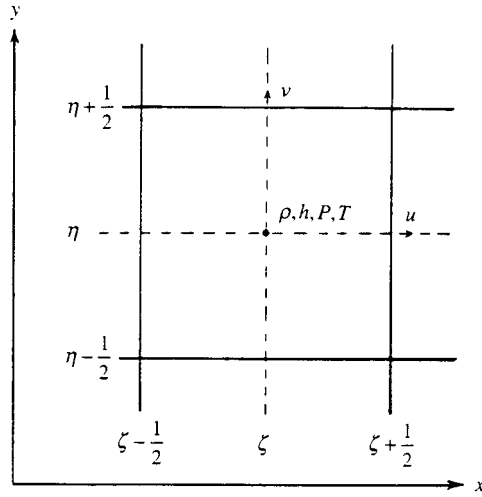


Figure 1. Finite difference grid notations and the locations of variables ρ , h , P , and T are located at the cell center; velocities u , v , and flux terms are at cell boundaries.

$$\frac{\partial D_j}{\partial P} = \frac{1}{(\partial P / \partial \rho_j)_{\zeta, \eta} \delta t} + \frac{\delta t [(\alpha_j)_{\zeta+1/2, \eta} + (\alpha_j)_{\zeta-1/2, \eta}]}{(\delta x)^2} + \frac{\delta t [(\alpha_j)_{\zeta, \eta-1/2} + (\alpha_j)_{\zeta, \eta+1/2}]}{(\delta y)^2} \quad (38)$$

The enthalpy equations were divided into two groups. The first group, including the heat transfer due to mass transfer, the interfacial sensible heat transfer, and the energy dissipation due to interfacial friction, is solved inside the pressure iteration loop. The second group, which contains the pressure compression work, shear stress dissipation energy, and the thermal diffusion, is solved outside the pressure iteration loop. A more detailed description of the numerical solution procedure is given in Lee [4]. An outline of a more stable, semi-implicit numerical scheme, which solves the two-fluid, six-equation model, is briefly described in Appendix C and generalized the above description. The jet impingement problem described in Section 5.3 was computed with both numerical schemes and found to produce the same results.

5. DESCRIPTION OF TEST PROBLEMS

This section describes each of the three test problems chosen for simulation.

5.1. Batch settling of a two-phase mixture

The first test problem consists of a single vertical column 0.1 m high and 0.01 m wide filled with a steam–water mixture of uniform vapor fraction $\alpha_j = 0.40$ at a pressure $P = 1.013 \times 10^5$ Pa and temperature $T = 373$ K. Ten finite difference cells were used, each 0.01 m high. The top and the bottom are closed so that no material enters or leaves the system. At time 0^+ , gravity

is switched on and liquid starts to settle to the bottom while vapor rises to the top. This is a thought problem, which tests the rate of phase separation and the ability to predict countercurrent flow. Fixed values of the interface drag function K were used and no mass transfer ($\Gamma_c = \Gamma_c = 0$).

5.2. One-dimensional fluidized bed (interfield drag experiment)

The experimental apparatus consisted in part of a vertical tubular glass column through which air is passed at known flow rates [18]. Initially, a bed of solid spherical particles rests on a fine mesh screen at the bottom of the tube. A flow-straightening section to minimize circumferential motion (swirling) of the gas is located in the entry section below the screen. As gas is passed through the particles, they are fluidized. Flow conditions, such as air flow rate, initial bed depth, and particle size and density were varied, and the behavior of the bed was recorded. For the flow conditions studied, the behavior of the bed is primarily a periodic slug flow or aggregate fluidization. An oscillatory period begins with the bed lifting off of the screen as a uniform mass. As it rises, it becomes more diffuse, and particles begin to drop off the bottom collecting on the screen forming the next slug. The upper boundary of the rising slug remains relatively flat. When the interparticle distance becomes great enough and the local fluid velocity is not sufficient to support the particles, the remaining slug falls, joining the lower slug as it is lifting off the screen.

Several experiments were carried out, but only one is simulated here. Motionless glass beads of 3 mm diameter (density = $2.2 \times 10^3 \text{ kg m}^{-3}$) initially fill the bottom 160 mm of the bed at a pressure of $1.013 \times 10^5 \text{ Pa}$, a temperature of 298 K, and a porosity $\alpha_j = 0.4$. The air is treated as an ideal gas. Twenty cells are used for a total system height of 1.6 m. Each cell is 80 mm wide and 80 mm high. At time 0^+ , the pure gas is introduced at 3 m s^{-1} and the pressure is reduced at the top to $7.72 \times 10^4 \text{ Pa}$ (atmosphere pressure in Los Alamos, NM). The solids velocity is set to zero at the bottom and top so that no glass beads leave the system. This simulation corresponds to the second run in Rexroth and Starkovich's Table I [18] for which a time-averaged voidage oscillation period of 0.89 s was obtained. We used the same drag function K as Rexroth and Starkovich [18].

5.3. Simulation of two-phase jet impinged on vertical plate

A horizontal two-phase, steam–water jet impinging on a vertical flat plate experiment [6] was also simulated. The experiment consisted of a round 10-mm tube discharging against a wall 5 mm away. The discharge conditions were recorded as pressure = $3.4 \times 10^6 \text{ Pa}$, temperature = 510.8 K, vapor volume fraction $\alpha_j = 0.67$, and mass flow rate = $3.055 \times 10^4 \text{ kg m}^{-2} \text{ s}^{-1}$. At time $t = 0^+$, the high-pressure jet containing the mixture of steam and water enters into a stagnant atmosphere and impinges on the vertical plate. On the plate, there are five stations recording the stagnation pressure. This experiment is simulated in three-dimensional Cartesian co-ordinates with ten cells in each of the x - and y -directions ($\delta x = \delta y = 5 \text{ mm}$), and five in the z -direction normal to the wall ($\delta z = 1 \text{ mm}$). Four cells were used in the jet. The total mass flow was set equal to the experimental value.

5.4. Results of computations and discussion

The purpose of the first test problem, the batch settling of a two-phase mixture, is to determine the effect of the interfacial drag on phase separation. From the computational experiment it was found that the drag function K has a lower limit of approximately $10 \text{ kg m}^{-3} \text{ s}^{-1}$. When using such a small value of K , the computation tends to become unstable. This instability is true for all five of the models. However, the instability is due to the numerical scheme used for solving the governing equations. Therefore, for a more stable finite difference method, the value of K may be less than 10. For large values of K , i.e., K is greater than about 1000, all models produce basically the same results. Figure 2 shows the transient void fraction for the top and bottom cells by using the basic set. With constant $K = 1000$, it takes approximately 0.21 s for the bottom cell to be filled with water and 0.3 s for the top cell to be filled with steam. For larger values of K , the separation rate decreases as expected, as shown in Figure 2. The transient vapor volume fractions for top and bottom cells are presented in Figure 3 for very early time for all the models. As indicated, all of the five models give basically the same results.

Figure 4 is a schematic of the experimental apparatus for the interfield drag experiment, whereas Figure 5 defines the modeling mesh and inflow, outflow, and internal boundary velocities. An artificial reduced flow area is imposed on the cell below the bed of glass beads so that a high air velocity can be obtained and consequently a non-negative particle velocity will be maintained. The maximum particle volume fraction oscillation period of 1.025 s and the

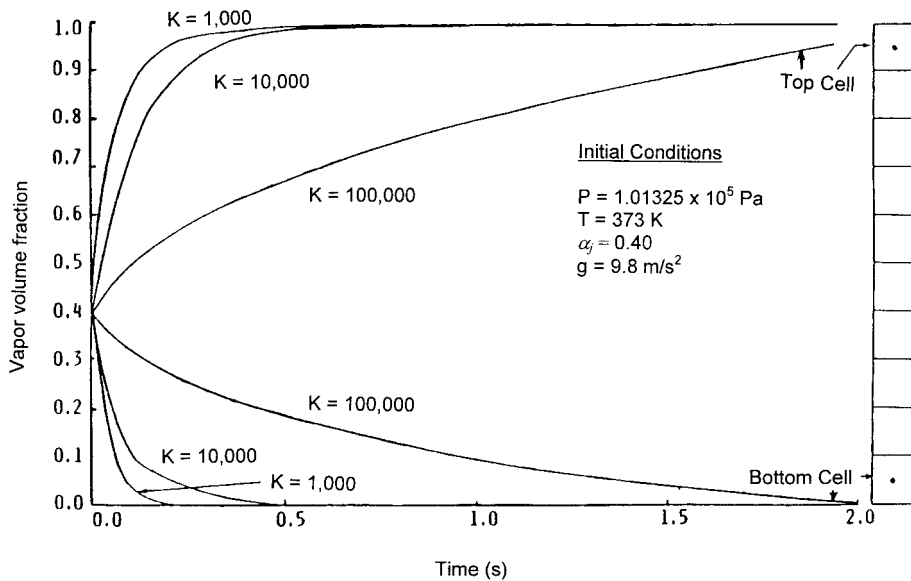


Figure 2. Transient vapor volume fraction for top and bottom cells using the basic set Equations (1)–(3a).

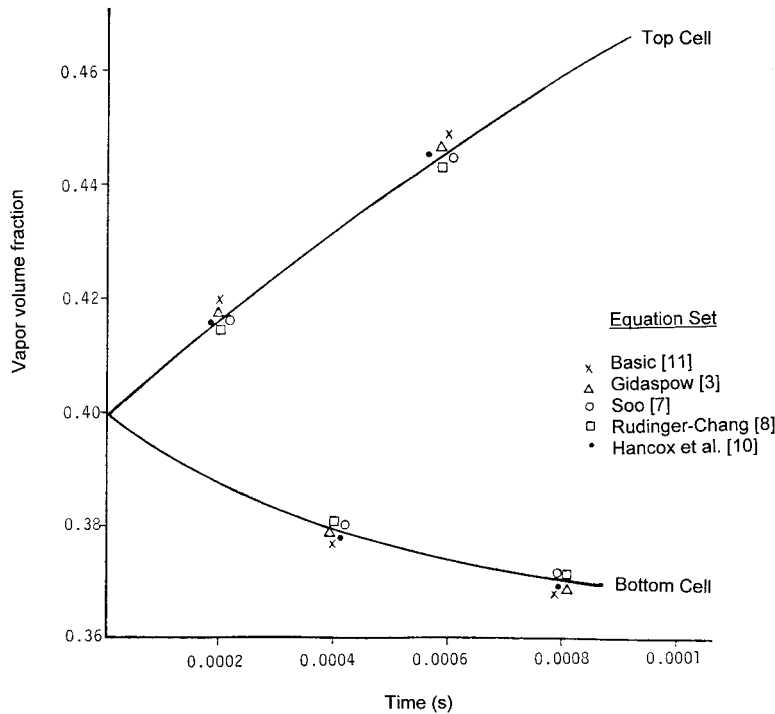


Figure 3. Transient vapor volume fraction for top and bottom cells in the very early time using all five models.

slug height of 0.64 m obtained by using the basic model are shown in Figure 6. The experimental data give a time-averaged oscillation period of 0.89 s and a height of 0.8 m. This discrepancy can be reduced by using a better drag function K . It was found that all models except Soo's give essentially the same oscillatory behavior but have a maximum slug height of about 25 per cent deviation from the basic set results. This deviation can be seen in Figure 7, which presents the transient particle volume fraction at the location of 0.2 m above the screen, i.e., the base of the glass bead bed initial height, for early time. It can be noticed that Soo's model produces results that deviate very much from the other models. It is not clear at this stage which term causes such a deviation but it is believed to be the inertial coupling terms [7]. Since these results are preliminary (as are all of them), a further investigation will be carried out in the near future to clarify such points. Hence the results are subject to change.

Figure 8 shows the experimental set-up and initial operating conditions for the two-phase jet impingement problem. The calculated results of the pressure distribution on the vertical plate by using the basic model are given in Figure 9 for different values of interfacial drag

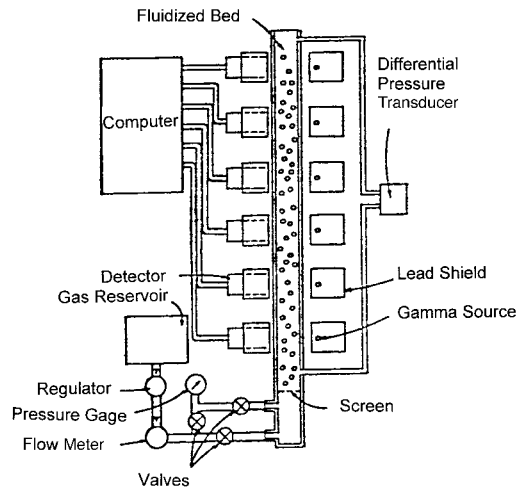


Figure 4. Apparatus for interfield drag experiment (adapted from Reference [18]).

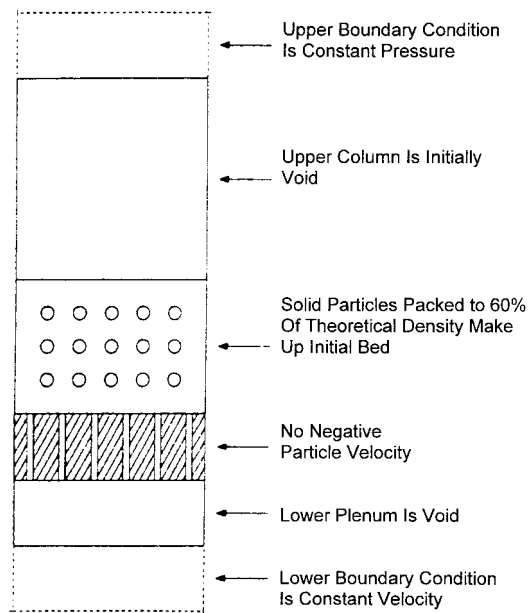


Figure 5. Calculational mesh set-up (adapted from Reference [18]).

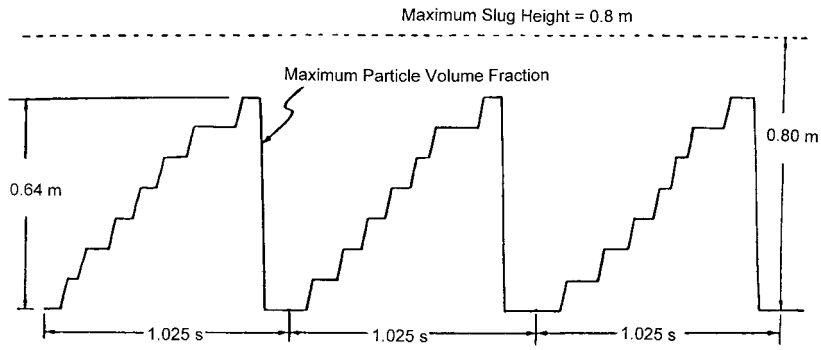


Figure 6. The particle oscillation period and the slug height.

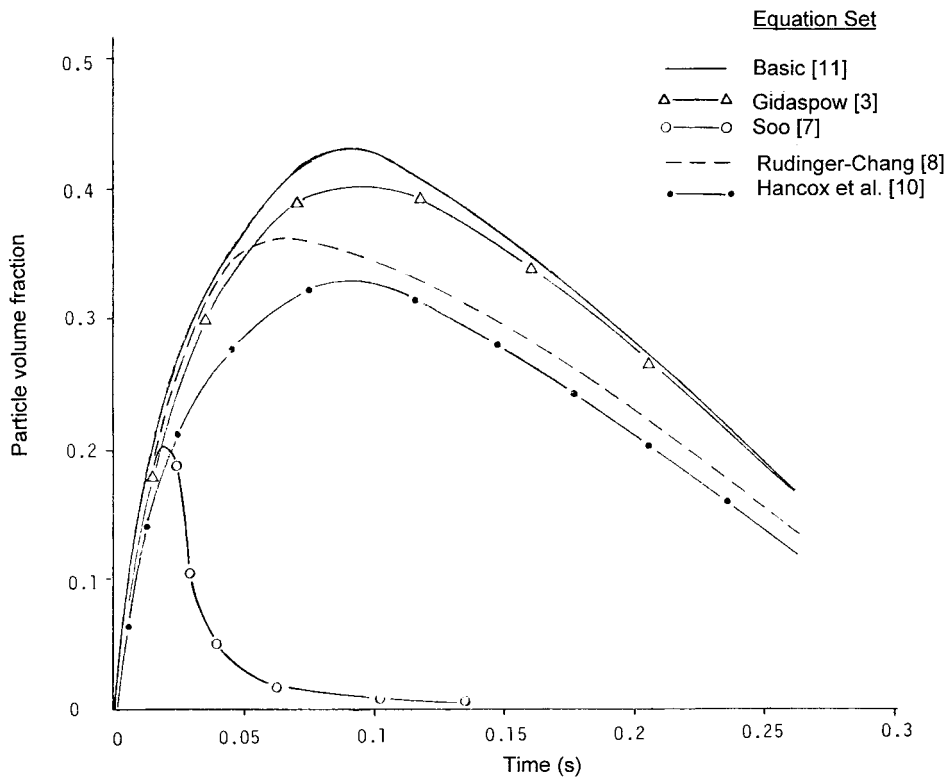


Figure 7. Transient particle volume fraction at 0.2 m above the screen.

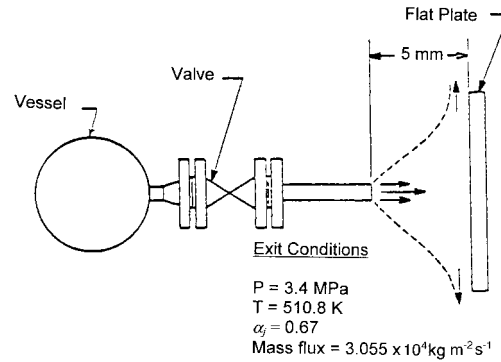


Figure 8. Two-phase jet impingement experiment (adapted from Reference [6]).

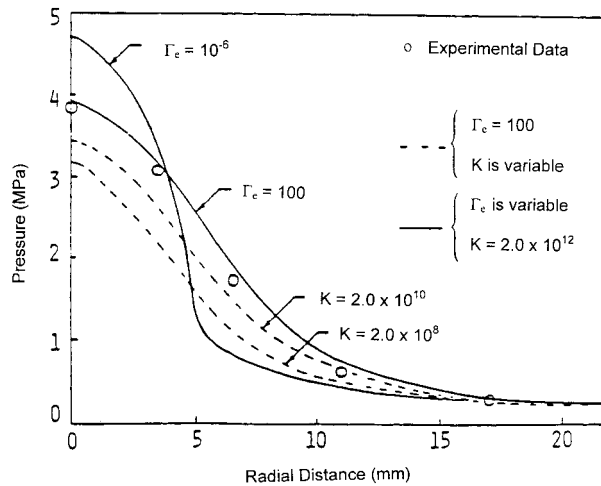


Figure 9. Basic model results as compared with experimental data.

function K and evaporation function Γ_e . The best simulations are obtained when $K = 2.0 \times 10^{12}$ and $\Gamma_e = 100$. The transient and steady state results of the pressure distribution for all models except the basic set are shown in Figure 10. At time $t = 50 \mu\text{s}$ and steady state, the models of Gidaspow, Soo, Rudinger–Chang, and Hancox *et al.* compute the same results. The steady state pressure distributions are very close to the measurements but not as good as the basic set as shown in Figure 9. It is interesting to note that at $t = 50 \mu\text{s}$, the results of the basic set are quite different from the other four models, with the basic set lying below the steady state pressure and the other four sets overshooting it.

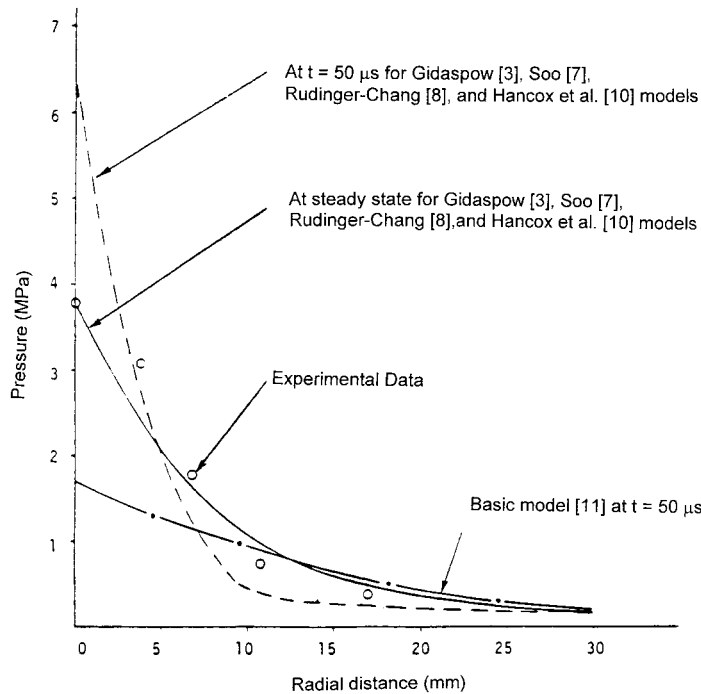


Figure 10. Computed results as compared with experimental data for all models.

6. CONCLUDING REMARKS

It is concluded that of the five models studied, four of them (basic [11], Gidaspow [3], Rudinger–Chang [8], and Hancox *et al.* [10]) are in close agreement with each other and the data for the low-pressure (0.1 MPa) fluidized bed experiment [18]. Soo's model [7] disagrees with the other four models and damps oscillations out, probably due to the presence of the inertial coupling terms. It is further concluded that all of the five models studied, four of them (Gidaspow [3], Soo [7], Rudinger–Chang [8], and Hancox *et al.* [10]) gave essentially the same results and are in very close agreement with the data for the high-pressure (3.4 MPa) jet impingement experiment [6]. All five models gave essentially the same results for the batch settling simulation.

A first-order finite difference scheme such as used herein to solve the governing equations introduces second-order numerical viscous stresses into the momentum equations when we discretize the differential equations. This will certainly change the stability for the numerical scheme of the two-phase flow equation sets. For example, Equations (1)–(3a) may become stable after discretization, depending on the grid size. It is also found that the models of Gidaspow [3] and Hancox *et al.* [10] are computationally slightly more unstable than the other three models because of the presence of the discretized time derivatives on the RHS of the momentum equations in the numerical schemes described in this paper.

ACKNOWLEDGMENTS

A portion of this work was accomplished at the Energy Technology and Energy Systems Division of Argonne National Laboratory, Argonne, Illinois, and supported by the U.S. Nuclear Regulatory Commission. Special thanks are due to Professor Dimitri Gidaspow, Department of Chemical Engineering Department, Illinois Institute of Technology, for stimulating and enlightening discussions during the preparation of the manuscript.

APPENDIX A. NOMENCLATURE

C_d	standard sphere drag coefficient
C_p	dynamic pressure coefficient (given by Equation (18))
C^*	defined by Equation (19a)
g	gravitational acceleration
h	specific enthalpy
k	heat conduction coefficient
K	drag function
N	number of particles per unit volume
P	pressure
r_p	radius of particle
R	exchange function describing heat transfer between fields
t	time
T	temperature
u	velocity in x -direction
u_m	mean velocity in x -direction defined by Equation (9)
\vec{U}	velocity vector, i.e. $\vec{U} = (u, v)$
v	velocity in y -direction
v_m	mean velocity in y -direction defined by Equation (10)
x	co-ordinate direction
y	co-ordinate direction

Greek letters

α	volume fraction
β	iteration step
δ	difference
$\lambda_1, \lambda_2, \lambda_3, \lambda_4$	eigenvalues used in Appendix B
λ_c, λ_e	relaxation parameters used in Equations (27) and (28)
η	cell index in y -direction
μ	dynamic viscosity
ω	relaxation factor
ρ	microscopic material density
ρ'	macroscopic material density, e.g., $\rho'_i = \alpha_i \rho_i$

ρ_m	mean density defined by Equation (11)
ρ^*	pseudo density defined by Equation (19b)
ζ	cell index in x -direction
Γ_c	condensation rate
Γ_e	evaporation rate

Subscripts

c	continuous phase
d	discontinuous phase
i	phase i = solid or liquid
j	phase j = gas or vapor
m	mean value
s	saturation state

APPENDIX B. CHARACTERISTICS FOR THE FIVE TWO-PHASE FLOW EQUATION SETS

1. For the basic equation set [19], the eigenvalues are

$$\lambda_{1,2} = -\frac{u_i \rho_i \alpha_j + u_j \rho_j \alpha_i}{\rho_i \alpha_j + \rho_j \alpha_i} \pm i \left[\frac{\rho_j \alpha_j \rho_i \alpha_i (u_i - u_j)^2}{(\rho_i \alpha_j + \rho_j \alpha_i)^2} \right]^{1/2} \quad (\text{B1})$$

and

$$\lambda_3^{-1} = \lambda_4^{-1} = 0$$

where

$$i = \sqrt{-1}$$

2. For Soo's momentum equations [7] with $c = 1$ and $b = 0$, the eigenvalues are

$$\lambda_{1,2}^{-1} = \frac{-b \pm (b^2 - 4ac)^{1/2}}{2a} \quad (\text{B2})$$

and

$$\lambda_3^{-1} = \lambda_4^{-1} = 0 \quad (\text{B3})$$

where

$$a = 1 + \frac{\alpha_i \rho_j}{\alpha_j \rho_i}$$

$$b = 2u_j \left(\frac{\alpha_i \rho_j}{\alpha_j \rho_i} + \frac{1}{\alpha_j} - \frac{u_i \alpha_j}{u_j \alpha_i} \right) \quad (\text{B4})$$

and

$$c = u_j^2 \left(\frac{\alpha_i \rho_j}{\alpha_j \rho_i} + \frac{1 + \alpha_i}{\alpha_j} - \frac{2u_i \alpha_i}{u_j \alpha_j} - \frac{P}{\alpha_j \rho_i u_j^2} \right) \quad (\text{B5})$$

The characteristics are real since

$$b^2 - 4ac = 4u_j^2 \left[\left(\frac{\alpha_i}{\alpha_j} \right)^2 \left(\frac{u_i}{u_j} - 1 \right)^2 + \frac{P}{\alpha_j \rho_i u_j^2} \left(1 + \frac{\alpha_i \rho_j}{\alpha_j \rho_i} \right) \right] > 0 \quad (\text{B6})$$

3. For the extended Rudinger and Chang momentum equations [9], the eigenvalues are

$$\lambda_1 = -u_j \quad (\text{B7})$$

and

$$\lambda_2 = \lambda_3 = \lambda_4 = -u_i \quad (\text{B8})$$

4. For the Hancox *et al.* momentum equations [10], the eigenvalues are

$$\lambda_{1,2} = u_m \pm v_m \quad (\text{B9})$$

and

$$\lambda_3 = \lambda_4 = 0 \quad (\text{B10})$$

Equation (B9) holds when u_d approaches u_c and the propagation velocities of interfacial waves are defined as

$$u_m = \{ \alpha_c \rho_d u_d + \alpha_d \rho_c u_c + [2u_d - \alpha_d (u_d - u_c)] C^* / 2 \} / \rho^* \quad (\text{B11})$$

and

$$v_m^2 = [(\rho^* + C^*) C_p \rho_c + \alpha_d^2 (C^*)^2 / 4 - \alpha_c \alpha_d \rho_c (\rho_d + C^*)] (u_c - u_d)^2 / (\rho^*)^2 \quad (\text{B12})$$

where C_p , C^* , and ρ^* are defined by Equations (18), (19a), and (19b) respectively.

5. For the Gidaspow's momentum equations [3], the eigenvalues are

$$\lambda_1^{-1} = \lambda_2^{-1} = \lambda_3^{-1} = 0 \quad (\text{B13})$$

and

$$\lambda_4^{-1} = \frac{\alpha_j \rho_i - \alpha_i \rho_j}{\alpha_i \rho_j u_j - \alpha_j \rho_i u_i} \quad (\text{B14})$$

APPENDIX C. A MORE STABLE NUMERICAL SCHEME

This Appendix gives an outline of a stable, semi-implicit numerical scheme, which calculates the pressure P and the vapor volume fraction α_j based on the following procedures:

1. Consider both vapor and liquid phases to be compressible.
2. Calculate the pressure P and vapor volume fraction α_j inside the iteration loop.
3. Compute the residue masses $(D_j)^\beta$ and $(D_i)^\beta$ from the continuity equations for vapor and liquid respectively, based on the iteration step β .
4. Use the relationships $D_j = D_j(P, \alpha_j)$, $D_i = D_i(P, \alpha_i)$, and the momentum equations to obtain

$$\frac{\partial D_j}{\partial P^\beta}, \frac{\partial D_i}{\partial P^\beta}, \frac{\partial D_j}{\partial \alpha_j^\beta}, \text{ and } \frac{\partial D_i}{\partial \alpha_j^\beta}$$

5. Solve $\partial P^{\beta+1} = P^{\beta+1} - P^\beta$ and $\partial \alpha_j^{\beta+1} = \alpha_j^{\beta+1} - \alpha_j^\beta$ from the following matrix:

$$\begin{bmatrix} \frac{\partial D_j}{\partial P^\beta} & \frac{\partial D_j}{\partial \alpha_j^\beta} \\ \frac{\partial D_i}{\partial P^\beta} & \frac{\partial D_i}{\partial \alpha_j^\beta} \end{bmatrix} \begin{bmatrix} \partial P^{\beta+1} \\ \partial \alpha_j^{\beta+1} \end{bmatrix} = \begin{bmatrix} -D_j^\beta \\ -D_i^\beta \end{bmatrix}$$

and then obtain the pressure $P^{\beta+1}$ and the vapor volume fraction $\alpha_j^{\beta+1}$.

6. The thermodynamic vapor density ρ_j is obtained from the equation of state $\rho_j = \rho_j(P, h_j)$ and liquid ρ_i from $\rho_i = \rho_i(P, h_i)$.
7. The macroscopic vapor density is $\rho'_j = \alpha_j \rho_j$, and that of liquid is $\rho'_i = \alpha_i \rho_i$.
8. Calculate the new vapor velocities $u_j^{t+\Delta t}$ and $v_j^{t+\Delta t}$ and the new liquid velocities $u_i^{t+\Delta t}$ and $v_i^{t+\Delta t}$ from the momentum equations.
9. Check the convergence, i.e., to see if $(D_j)^\beta < \varepsilon_1$ and $(D_i)^\beta < \varepsilon_2$, where ε_1 and ε_2 are some specified small numbers.

10. If step 9 is satisfactory, then, the calculation is finished, otherwise, it should go back to step 3 for new iteration until it converges or stops at some desired iteration step, e.g., iteration = 100.
11. After step 10 is done, the energy equations will be used to calculate the enthalpies h_j and h_i .

The detailed derivations of the matrix coefficients appearing in step 5 are given in Reference [4].

REFERENCES

1. Stuhmiller JH. The influence of interfacial pressure forces on the character of two-phase flow model equations. *International Journal for Multiphase Flow* 1977; **3**: 551–560.
2. Banerjee S, Ferch RL, Mathers WG, McDonald BH. The dynamics of two-phase flow in a duct. In *Sixth International Heat Transfer Conference, Toronto, Canada, 7–11 August; General Papers*, vol. 1, Rogers JT (ed.). Hemisphere Publishing: Washington, 1978; 345–350, Paper No. FB-13.
3. Gidaspow D. A set of hyperbolic incompressible two-phase flow equations for two components. In *Heat Transfer Research and Application AIChE Symposium Series, No. 174*, vol. 74, Chen JC (ed.). American Institute of Chemical Engineers: New York, 1978; 186–190.
4. Lee WH. A pressure iteration scheme for two-phase flow modeling. In *Multiphase Transport Fundamentals, Reactor Safety, Applications*, vol. 1, Veziroglu TN (ed.). Hemisphere Publishing: Washington, DC, 1980; 407–431.
5. Soo SL. *Multiphase Fluid Dynamics*. Gower Technical: Beijing, 1990; 367–372. Distributed by Ashgate Pub. Co., Brookfield, VT.
6. Schweickert H. Untersuchung der Vorgänge in einem mehrfach unterteilten Containment beim Bruch einer Kuhlmitteleitung Wassergekühlter Reaktoren. Technischer Bericht BFR 50-32-C12-1, Kraftwerk Union, Germany, 1976.
7. Soo SL. Equations of multiphase–multidomain mechanics. In *Multiphase Transport Fundamentals, Reactor Safety, Applications*, vol. 1, Veziroglu TN (ed.). Hemisphere Publishing: Washington, DC, 1980; 291–305.
8. Rudinger G, Chang A. Analysis of non-steady two-phase flow. *Physics of Fluids* 1964; **7**: 1747–1754.
9. Lyczkowski RW. Transient propagation behavior of two-phase flow equations. In *Heat Transfer: Research and Application, AIChE Symposium Series, No. 174*, vol. 74, Chen JC (ed.). American Institute of Chemical Engineers: New York, 1978; 165–174.
10. Hancox WT, Ferch RL, Liu WS, Nieman RE. On one-dimensional models for transient gas–liquid flow in ducts. *International Journal for Multiphase Flow* 1980; **6**: 25–40.
11. Lyczkowski RW, Gidaspow D, Solbrig CW, Hughes ED. Characteristics and stability analyses of transient one-dimensional two-phase flow equations and their finite difference approximations. *Nuclear Science and Engineering* 1978; **66**(3): 378–396.
12. Los Alamos Scientific Laboratory. TRAC-P1: an advanced best estimate computer program for PWR LOCA analysis. Los Alamos Scientific Laboratory Report NUREG/Cr-0063, LA-7279-MS, Vol. I. Los Alamos, NM, June, 1978.
13. Arastoopour H, Gidaspow D. Vertical pneumatic conveying using four hydrodynamic models. *Industrial Engineering and Fundamentals* 1979; **18**: 123–130.
14. Shih YT, Arastoopour H. Hydrodynamic analysis of horizontal solids transport. *Industrial Engineering and Fundamentals* 1980; **21**: 37–43.
15. Lee WH, Shah VL. Numerical simulation for two-phase jet problem. In *Numerical Methods in Laminar and Turbulent Flows, Proceedings of the 2nd International Conference*, Venice, Taylor C, Schrefler BA (eds). Pineridge Press: UK, 1981; 841–852.
16. Lee WH, Lyczkowski RW. Development of a state of the Art Reactor Containment Program. In *17th National Heat Transfer Conference*, Salt Lake City, UT [preprints of AIChE Papers], Small WM (ed.). American Institute of Chemical Engineers: New York, 1977; 130–138.
17. Solbrig CW, McFadden JH, Lyczkowski RW, Hughes ED. Heat transfer and friction correlations required to describe steam–water behavior. In *Nuclear Safety Studies, Heat Transfer Research and Applications, AIChE Symposium Series No. 174*, vol. 74, Chen JC (ed.). American Institute of Chemical Engineers: New York, 1978; 100–128.
18. Rexroth PE, Starkovich VS. Measurement and analysis. In *Multi-Phase Flow Systems, Multiphase Transport Fundamentals, Reactor Safety, Applications*, vol. 5, Veziroglu TN (ed.). Hemisphere Publishing: Washington, DC, 1980; 2469–2481.
19. Lyczkowski RW, Gidaspow D, Solbrig CW. Multiphase flow models for nuclear, fossil, and biomass energy production. In *Advances in Transport Processes*, vol. 2, Majumdar AS, Mashelkar RA (eds). Wiley Eastern: New Delhi, 1982; 198–340.